Author Manuscript
Accepted for publication in a peer-reviewed journal
NIST National Institute of Standards and Technology • U.S. Department of Commerce

Published in final edited form as:
ECS Trans. 2015 ; 69(7): 147–157. doi:10.1149/06907.0147ecst.

New Insights into Sequential Infiltration Synthesis

Jeffrey W. Elam[a], **Mahua Biswas**[a], **Seth B. Darling**[a], **Angel Yanguas-Gil**[a], **Jonathan D. Emery**[a], **Alex B. F. Martinson**[a], **Paul F. Nealey**[a,b], **Tamar Segal-Peretz**[b], **Qing Peng**[c], **Jonathan Winterstein**[d], **J. Alexander Liddle**[d], and **Yu-Chih Tseng**[e]

[a]Argonne National Laboratory, Argonne, IL 60439, USA

[b]University of Chicago, Chicago, IL 60637, USA

[c]Duke University, Durham, NC 27708, USA

[d]National Institute of Standards and Technology, Gaithersburg, MD 20899, USA

[e]CanmetMATERIALS, Hamilton, Ontario L8P 0A5, Canada

Abstract

Sequential infiltration synthesis (SIS) is a process derived from ALD in which a polymer is infused with inorganic material using sequential, self-limiting exposures to gaseous precursors. SIS can be used in lithography to harden polymer resists rendering them more robust towards subsequent etching, and this permits deeper and higher-resolution patterning of substrates such as silicon. Herein we describe recent investigations of a model system: Al_2O_3 SIS using trimethyl aluminum (TMA) and H_2O within the diblock copolymer, poly(styrene-block-methyl methacrylate) (PS-b-PMMA). Combining in-situ Fourier transform infrared absorption spectroscopy, quartz-crystal microbalance, and synchrotron grazing incidence small angle X-ray scattering with high resolution scanning transmission electron microscope tomography, we elucidate important details of the SIS process: 1) TMA adsorption in PMMA occurs through a weakly-bound intermediate; 2) the SIS kinetics are diffusion-limited, with desorption 10× slower than adsorption; 3) dynamic structural changes occur during the individual precursor exposures. These findings have important implications for applications such as SIS lithography.

Introduction

Sequential infiltration synthesis (SIS) is a technique in which a polymer is infiltrated with inorganic material using alternating, self-limiting exposures of the polymer to a pair of precursor vapors(1–5). SIS is similar in many respects to atomic layer deposition (ALD) except that there is no substrate surface upon which a film grows. Instead, the SIS materials nucleate on functional species (such as carbonyl groups, C=O) within the polymer bulk, and these nucleation sites act as seeds for the subsequent growth of inorganic particles within the polymer. The result is an organic/inorganic hybrid material where the inorganic loading is controlled by the number of SIS cycles performed. The organic material can be burned or etched away to leave only the inorganic material, thereby providing a polymer-templated synthetic route for creating nanostructured materials.

NIST Author Manuscript
NIST Author Manuscript
NIST Author Manuscript

NIST Author Manuscript NIST Author Manuscript NIST Author Manuscript

One very promising application for SIS is lithography. Lithographic etching is a core technology in microelectronics manufacturing. As feature sizes continue to shrink according to Moore's law, the characteristic dimensions of the polymer resists, such as the line width and spacing, must be made smaller. If the thickness of the resist film is kept constant, then the aspect ratio (height/width) of the polymer features increases, and this can lead to problems such as domain collapse. Alternatively, if the resist thickness is reduced to combat this problem, then the polymer becomes too fragile for the plasma etch, and this limits how deeply the underlying substrate can be patterned. Intermediate hard masks can help alleviate this problem, but hard masks increase cost and complexity, and can increase line edge roughness. Alternatively, the polymer resist can be made more robust using SIS. For instance, SIS can increase the etch depth by up to 37–57× compared to conventional resists in electron beam- and photo-lithography(3,5) (Fig. 1).

Another exciting aspect of SIS is the selective infiltration of block copolymers (BC). BC are composed of two or more polymers covalently linked together. For instance, poly(styrene-block-methyl methacrylate) (PS-b-PMMA) is a diblock copolymer composed of polymer strands which each have a PS section linked to a PMMA section. The immiscibility of the PS and PMMA components causes a spontaneous phase segregation to form a mesoscopic pattern where the morphology (e.g. spheres, cylinders, or lamella) are controlled by the PS/PMMA ratio, and the characteristic size scale (e.g. diameter of spheres, spacing between cylinders) are dictated by the molecular weight of the polymer. Given the chemistry-specific nature of the polymer-precursor interaction in SIS, it is possible to selectively infiltrate only one of the two components. For instance, trimethyl aluminum (TMA) will react exclusively with PMMA, but not with the PS. As a consequence, aluminum oxide SIS using TMA and H_2O will only affect the PMMA component. When the polymer is burned or etched away, the remaining Al_2O_3 will assume the pattern of the PMMA component of the PS-b-PMMA mesostructure. The library of ALD chemistries combined with the wealth of BC materials render the combination of SIS and BC a flexible and promising route for the synthesis of inorganic nanophase materials. SIS of Al_2O_3, SiO_2, ZnO, TiO_2, and W have been demonstrated(2).

Recently, BC materials have emerged as a means for extending lithographic patterning below the diffraction limit through a process called directed self-assembly (DSA)(6). In DSA, chemical pre-patterns are defined using traditional lithography, and these patterns are used to direct the self-assembly of the BC such that they align with the patterns. These BC can then be used as an etch resist, and the net result is to increase the pattern density by ×4 or greater. DSA is an ideal application for SIS since the selective chemistry ensures that the inorganic material will infiltrate only one component, and the added etch-resistance allows for much deeper patterning.

Given the potential utility for SIS in nanofabrication and lithography, it is worthwhile to study this process in detail to achieve greater control and predictive power. To this end, we have employed a range of characterization tools to investigate SIS. In this paper we focus mostly on the prototypical Al_2O_3 SIS process using TMA/H_2O into PS-b-PMMA, and we highlight recent results obtained using in-situ Fourier transform infrared absorption spectroscopy, in-situ quartz crystal microbalance, in-situ synchrotron grazing incidence

NIST Author Manuscript
NIST Author Manuscript
NIST Author Manuscript

small angle X-ray scattering, and high resolution scanning transmission electron microscope tomography.

Experimental

PMMA films of ~60 nm thickness were used as model resist layers for most of the in situ FTIR studies(7,8). The sample substrates consisted of IR-transparent Si coupons with the native SiO_2 intact, which were cleaned in isopropyl alcohol (IPA). The PMMA films were deposited onto the Si by spin casting using a 2 wt.% solution of 950 K molecular weight PMMA in anisole (Micro Chem). After deposition, the PMMA films were annealed at 180 °C for 180 s on a hot plate to evaporate the solvent. In situ FTIR measurements were performed in transmission mode using a Nicolet 6700 FTIR spectrometer (Thermo Scientific) interfaced to a custom ALD reactor.(9,10) A transmission spectrum was recorded from an identical, bare Si substrate for use as the background. The PMMA-coated substrates were allowed to equilibrate in flowing, ultra-high-pure (UHP, 99.999%) N_2 using a 300 sccm flow rate at 3.5 Torr pressure within the heated reactor for 30 minutes before commencing the SIS experiments.

Al_2O_3 SIS used alternating exposures to TMA (Aldrich, 97%) and deionized H_2O and was performed in flow mode, whereby the precursor vapors were introduced into a steady, 300 sccm flow of N_2 carrier gas that swept through the ALD reactor. The base pressure of N_2 without precursors was 3.5 Torr. Using a predetermined exposure period, 6 Torr TMA was admitted into the reactor after which the TMA dosing valve was closed, and pure N_2 gas flowed through the reactor at 3.5 Torr for a predetermined purge period. Most of the FTIR experiments used 180 s dose times for both precursors since virtually no further changes in the FTIR spectra were observed using longer dose times. Each FTIR spectrum is an average of 256 scans recorded at a resolution of 4 cm^{-1} over 320 s. The SIS substrate temperature was maintained at 85 °C using a temperature-controlled stage. The reactor walls were maintained at approximately the same temperature as the substrate to prevent precursor condensation.

Titanium tetrachloride ($TiCl_4$, Aldrich, 99.9%) was used along with H_2O for performing TiO_2 SIS at 135 °C, and in situ quartz crystal microbalance (QCM) measurements were performed using sensors that had been pre-coated with polymer films. PS and PMMA films were prepared by spin coating at 3000 rpm from a 2.5 wt % toluene solution, and dried on a hot plate at 120°C. PS-b-PMMA (Mw = 50,500/20,900) was purchased from Polymer Source Inc. and purified through Soxhlet extraction to remove excess PS homopolymer before spin coating. After deposition, the PS-b-PMMA films were annealed at 250°C for two hours in a vacuum oven, then cooled to room temperature to obtain self-assembled patterns. The in-plane PMMA cylinders were 30 ±3 nm in diameter, and the center-to-center lateral distance was 60 ±5 nm. The crystal was then sealed into the QCM fixture using epoxy. Polished QCM crystal sensors with an Au coating (Colorado Crystal Corp.) were mounted in the Maxtek BSH-150 bakeable sensor head and the mass changes were measured using a Maxtek TM-400 thickness monitor(11).

NIST Author Manuscript

NIST Author Manuscript

NIST Author Manuscript

Results and Discussion

In Situ FTIR Measurements

Figure 2 shows in situ FTIR spectra recorded during Al_2O_3 SIS into PMMA referenced to a clean silicon substrate. The features of interest are the carbonyl (C=O) at 1729 cm^{-1} and the ester (C-O-R) stretching at 1260 cm^{-1} The TMA spectrum is referenced to the PMMA spectrum to highlight the spectral changes that occur upon TMA exposure. Similarly, the H_2O spectrum is referenced to the TMA spectrum. Following the TMA exposure, negative features emerge at 1729 and 1260 cm^{-1}, suggesting the consumption of carbonyl and ester groups, respectively, and positive features appear consistent with adsorbed TMA: CH stretching of Al-CH_3 at 2923 cm^{-1} and CH rocking of Al-CH_3 at ~700 cm^{-1}. In addition, new positive features are seen at 1670 and 1297 cm^{-1}. The H_2O exposure removes all of the CH peaks associated with the TMA methyl groups, while simultaneously reversing the peak shifts for the C=O and C-O-R peaks produced by the TMA. The complete TMA-H_2O SIS cycle generates an increase in the Al-O phonon mode at ~800 cm^{-1} due to Al_2O_3 formation(13), but this feature is only visible if the post-H_2O dose spectrum is referenced to PMMA (not shown).

To evaluate the saturation behavior of the spectral changes associated with the TMA exposures in Fig. 2, a series of spectra were recorded after different TMA exposure times ranging from 50s to 240s, and the C=O and Al-CH_3 peaks were integrated after each measurement. The results are shown in Fig. 3. Figure 3 appears to show that the TMA reaction with PMMA saturates after ~240s. However, much longer TMA exposures of up to 3 hours continued to show an increase in the Al-CH_3 peak even though the C=O feature remained constant. In addition, the Al-O peak at ~800 cm^{-1} continued to rise along with the Al-CH_3 peak suggesting additional TMA uptake without the consumption of additional C=O. Furthermore, most of the spectral changes induced by the TMA exposure in Fig. 2 reversed slowly if the TMA purge time was extended from 35 s to 60 min. These finding reveal that TMA adsorption is more complex than simple chemisorption to C=O sites and suggest a two-step adsorption mechanism (Fig. 4). In step 1, TMA reacts quickly to form a weakly-bound intermediate. This interaction is signaled by the shift in C=O and C-O-R features, indicative of weakly bound donor-acceptor complexes.(14) This intermediate can either desorb, or proceed to react to form a permanent Al-O linkage (step 2). This two-step model has important implications for SIS lithography: longer TMA exposure times and shorter TMA purge time produce a higher concentration of covalently bound Al-O, and this in turn produces a more robust resist permitting deeper patterning(7).

We next studied the kinetics of the Al_2O_3 SIS into PMMA using in situ FTIR by measuring the time-dependence of TMA absorption at 85°C. These studies used PMMA film thicknesses of 35, 60, and 120 nm on silicon, and a constant TMA purge time of 355s. The decrease in intensity for the C=O at 1729 cm^{-1} was monitored by FTIR versus TMA exposure time for each film, and the resulting plots of integrated C=O intensity versus TMA exposure time were fit using the function: $y=A[1-\exp(-t/\tau_a)]$ where y is the IR absorbance, t is the TMA exposure time, A is a fitting constant, and τ_a is an effective time constant for adsorption. The square symbols in Fig. 5 show the τ_a values obtained from this fitting

NIST Author Manuscript NIST Author Manuscript NIST Author Manuscript

process versus PMMA film thickness, and the solid line shows a fit to these data using: $\tau_a = BT^2$ where B is a fitting constant and T is the film thickness. The excellent fit to the T^2 behavior is consistent with adsorption being a diffusion-limited process. However, since adsorption and desorption happen concurrently during the TMA infiltration of the PMMA, the τ_a values are expected to depend on both the diffusivity and the adsorption kinetics (i.e. the bond strength of the C=O···TMA intermediate complex shown in Fig. 4). We also note that the fraction of C=O species consumed from the PMMA was in the range of 5–6% regardless of the PMMA film thickness (these calculations were performed after long TMA purge and subsequent H_2O exposure to eliminate the effects of TMA desorption from the measurements). The independence of fractional C=O consumption with thickness confirms that SIS is a bulk process and occurs throughout the film in a homogenous fashion so long as the exposure time is sufficient to achieve saturation.

Next we measured the desorption kinetics for TMA from PMMA by performing a similar set of experiments to those described above, but with a constant TMA exposure time of 180s and varying TMA purge times. We generated plots of C=O intensity versus TMA purge time for each of the three PMMA film thicknesses, and fit these data with an exponential decay: $y=10*\exp(-t/\tau_d)$ where y is the IR absorbance, t is the TMA purge time and τ_d is an effective time constant for desorption. The round symbols in Fig. 5 show the τ_d values obtained from this fitting process versus the PMMA film thickness, and the solid line shows a fit to these data using: $\tau_d = CT^2$ where C is a fitting constant and T is the film thickness. As with the adsorption data described above, the TMA desorption data fit well to a T^2 function indicating that desorption is diffusion-limited. The effective desorption time constants combine the decomplexation kinetics and the diffusion kinetics of TMA out of the film since both processes are occurring simultaneously. We note that the τ_d values are ~10 times larger than the corresponding τ_a values, suggesting a larger kinetic barrier for desorption compared to adsorption. Examination of the FTIR spectra revealed that a small portion of the C=O is permanently removed. These C=O species are consumed during the reaction of TMA with PMMA to form Al-O, as evidenced by an Al-O peak at ~800 cm^{-1} that appears during the TMA purge times. This effect is magnified using longer TMA exposures.(7) The practical importance of the TMA purge time for PS-b-PMMA BCP lithography is that more complete and well-defined Al_2O_3 patterns are achieved in fewer SIS cycles using shorter TMA purge times.

In Situ QCM Measurements

Next we investigated TiO_2 SIS using $TiCl_4$ and H_2O. We used in-situ QCM measurements to examine TiO_2 SIS in PS (180 nm), PMMA (240 nm), and PS-b-PMMA (280 nm) films and the results are summarized in Fig. 6. Given that TMA and $TiCl_4$ are both Lewis acids, we might expect that these two compounds would react similarly with polymers. For instance, PS is composed of only C and H, so there are no electron-donating functional groups to react with the Lewis acidic $TiCl_4$. Indeed, the mass changes observed during TiO_2 SIS in PS are very small as shown by the triangles in Fig. 6. For comparison, the dashed line shows the expected mass changes of 19 ng/cm^2 for TiO_2 ALD on a planar surface under these conditions. In contrast, the first TiO_2 SIS cycle in PMMA produced a very large mass gain of 1400 ng/cm^2 (square symbols in Fig. 6), equivalent to ~74× the growth observed on

NIST Author Manuscript NIST Author Manuscript NIST Author Manuscript

planar surfaces. Evidently, the C=O and C-O-R polar species react with the electropositive $TiCl_4$ just as they do with TMA. The mass changes decrease with increasing number of TiO_2 SIS cycles, and by 7 cycles the values are similar to the expected mass changes on a planar surface, suggesting that the SIS TiO_2 has filled the void spaces in the PMMA necessary for diffusion into the bulk.

Finally, the diamond symbols in Fig. 6 show the mass changes observed during TiO_2 SIS into the PS-b-PMMA film. The initial SIS cycles produce very large mass changes similar to those seen with PMMA. Unlike the behavior on pure PMMA however, the large mass gains persist even after 7 SIS cycles. Evidently, the $TiCl_4$ and H_2O are able to diffuse into the film even after the PMMA voids have been blocked. A likely explanation for this behavior is that the PS component of the PS-b-PMMA film continues to provide a fast diffusion pathway for the SIS precursors to reach unreacted C=O and C-O-R species in the PMMA. Since the PS is inert towards the $TiCl_4$ and H_2O, the void spaces in the PS will remain open. This mechanism should permit a higher loading of inorganic material via SIS in the PS-b-PMMA films allowing more robust resists and deeper etching.

In Situ GISAXS Measurements

Grazing incidence small angle scattering (GISAXS) is a powerful technique for characterizing structural changes in soft matter films such as BC (15). To gain additional insight into the SIS mechanism, we performed Al_2O_3 SIS while recording in situ GISAXS data continuously over 5 SIS cycles. This study was conducted at beamline 12-ID-C at the Advanced Photon Source, Argonne National Laboratory, using a custom-built portable ALD reactor outfitted with a GISAXS-specific deposition cell. In this section we will briefly highlight some of the findings from our study.

Figure 7(a) shows scattering data prior to the SIS process. This image possesses specular diffuse scattering at in-plane momentum transfer $q_y = 0$, as well as symmetrical pairs of 1st and 3rd order Bragg rods at $q_y = \pm 0.0228$ Å^{-1} and 0.0684 Å^{-1}, respectively. The position of these rods correlate to a lamellar pitch of 27.6 nm, in good agreement with the expect pitch of 30 nm. Prior to SIS, the 2nd order Bragg rod – expected at $q_y = 0.0556$ Å^{-1} – is not observed, indicating that the PS and PMMA domains are of equal lateral dimension which leads to a symmetry-forbidden 2nd order Bragg rod. Figure 7(b) shows GISAXS data from the same film after 5 Al_2O_3 SIS cycles. It is clear that the overall scattered intensity in the Bragg rods has increased, indicating an enhancement in the electron density difference between the PMMA and PS domains, as expected for the selective reaction of the TMA with the PMMA. In addition, we observe the emergence of the 2nd order Bragg rod at $q_y = 0.0556$ Å^{-1}, indicating that the two polymer domains no longer have the same lateral dimensions. This data also corroborates the selective growth of SIS Al_2O_3 in the PMMA, which would cause the PMMA to swell and intrude into the PS domains, thereby breaking the symmetry. We note that the position of the Bragg rods themselves do not shift in q_y, indicating that the Al_2O_3 SIS does not alter the pitch of the lamellae, in agreement with previous studies(1). Finally, we see a distinct increase in diffuse scattering at higher q than the Bragg rods consistent with the formation of nanoparticles. A Guinier approximation assuming spherical nanoparticles indicates a radius of ~1.5 nm. Figure 7 shows only two snapshots from the

NIST Author Manuscript

NIST Author Manuscript

NIST Author Manuscript

time-dependent GISAXS data recorded continuously over the 5 SIS cycles (not shown). Detailed examination of the full data set (not shown) reveals slow transient behavior during the TMA purges consistent with desorption from the physisorbed complex (Fig. 4) as well as infiltration waves consistent with the top-to-bottom modification of the polymer film during the precursor exposures.

HRTEM Tomography

Understanding and controlling the three-dimensional structure of BCP thin films is critical for utilizing these materials in lithography. Scanning transmission electron microscopy (STEM) is an effective tool for evaluating the structure of nanomaterials, but the low contrast between the different domains in the BCP films makes this difficult. Recently, we discovered that Al_2O_3 SIS can greatly improve the contrast between the BCP domains in STEM, enabling STEM tomography for three-dimensional (3D) characterization of BCP films(16). For instance, Fig. 8 shows 3D STEM tomographic data recorded from an Al_2O_3 SIS-treated cylinder-forming BCP film. Figure 8a shows an xy slice from the 3D data set and the arrow points to a splitting defect ("inverted Y" structure) where a single cylinder at the top of the film splits into two cylinders towards the bottom of the film. In addition, the 3D visualization of the same region shown in Fig. 8b illustrates how the cylinders surrounding the splitting defect bend to accommodate the change in spacing. Pattern defects will hamper the incorporation of BCP lithography into semiconductor manufacturing, but the ability to visualize these defects in high resolution is a critical first step towards controlling and eventually eliminating them.

Conclusions

SIS shares much in common with ALD, so that the vast library of ALD chemistries are in principle transferrable to SIS and should enable advances in both nanomaterials synthesis and lithography. However, compared to the well-defined surfaces inherent to ALD, nucleation during SIS occurs on functional groups within an organic matrix and this introduces additional complexities such as slow diffusion through the polymer free volume and molecular confinement by the polymer chains. Fortunately, many of the in situ diagnostic techniques developed for ALD, such as FTIR and QCM, can be utilized in SIS to understand these complex phenomena. We have demonstrated that FTIR can provide direct information about the polymer-precursor interaction, and QCM gives details about diffusion and reaction within the polymer matrix. Furthermore, new techniques can also help illuminate the SIS process: in situ GISAXS can capture structural changes in real time, and 3D STEM tomography can pin-point defects within a BCP film. There is still much to be learned about SIS, but the potential applications in nanomanufacturing and lithography are certain to stimulate continued research in this exciting field.

Acknowledgments

JWE and SBD are grateful to the Argonne Technology Development and Commercialization Division for funding through a Technology Maturation Grant. This work was supported as part of the ANSER Center, an Energy Frontier Research Center funded by the U.S. Department of Energy, Office of Science, Office of Basic Energy Sciences, under Award number DE-SC001059. Use of the Advanced Photon Source (12–ID) was supported by the U. S.

Department of Energy, Office of Science, Office of Basic Energy Sciences, under Contract No. DE-AC02-06CH11357.

References

1. Peng Q, Tseng YC, Darling SB, Elam JW. Adv. Mater. 2010; 22(45):5129. [PubMed: 20827673]
2. Peng Q, Tseng YC, Darling SB, Elam JW. ACS Nano. 2011; 5(6):4600. [PubMed: 21545142]
3. Tseng YC, Peng Q, Ocola LE, Czaplewski DA, Elam JW, Darling SB. J. Vac. Sci. Technol. B. 2011; 29:6.
4. Tseng YC, Peng Q, Ocola LE, Czaplewski DA, Elam JW, Darling SB. J. Mater. Chem. 2011; 21(32):11722.
5. Tseng YC, Mane AU, Elam JW, Darling SB. Adv. Mater. 2012; 24:2608. [PubMed: 22488639]
6. Liu C-C, Ramirez-Hernandez A, Han E, Craig GSW, Tada Y, Yoshida H, Kang H, Ji S, Gopalan P, de Pablo JJ, Nealey PF. Macromolecules. 2013; 46(4):1415.
7. Biswas M, Libera JA, Darling SB, Elam JW. Chemistry of Materials. 2014; 26(21):6135.
8. Biswas M, Libera JA, Darling SB, Elam JW. J. Phys. Chem. C. 2014; 119:14585.
9. Comstock DJ, Elam JW. J. Phys. Chem. C. 2013; 117(4):1677.
10. Goldstein DN, McCormick JA, George SM. J. Phys. Chem. C. 2008; 112(49):19530.
11. Elam JW, Groner MD, George SM. Rev. Sci. Instrum. 2002; 73(8):2981.
12. Thurn-Albrecht T, Steiner R, DeRouchey J, Stafford CM, Huang E, Bal M, Tuominen M, Hawker CJ, Russell T. Adv. Mater. 2000; 12(11):787.
13. Frederick BG, Apai G, Rhodin TN. Physical Review B. 1991; 44(4):1880.
14. Pasynkiewicz S. Pure and Applied Chemistry. 1972; 30(3–4):509.
15. Hexemer A, Muller-Buschbaum P. Iucrj. 2015; 2:106. [PubMed: 25610632]
16. Segal-Peretz T, Winterstein J, Doxastakis M, Ramirez-Hernandez A, Biswas M, Ren J, Suh HS, Darling SB, Liddle JA, Elam JW, de Pablo JJ, Zaluzec NJ, Nealey PF. ACS Nano. 2015; 9(5):5333. [PubMed: 25919347]

NIST Author Manuscript NIST Author Manuscript NIST Author Manuscript

NIST Author Manuscript
NIST Author Manuscript
NIST Author Manuscript

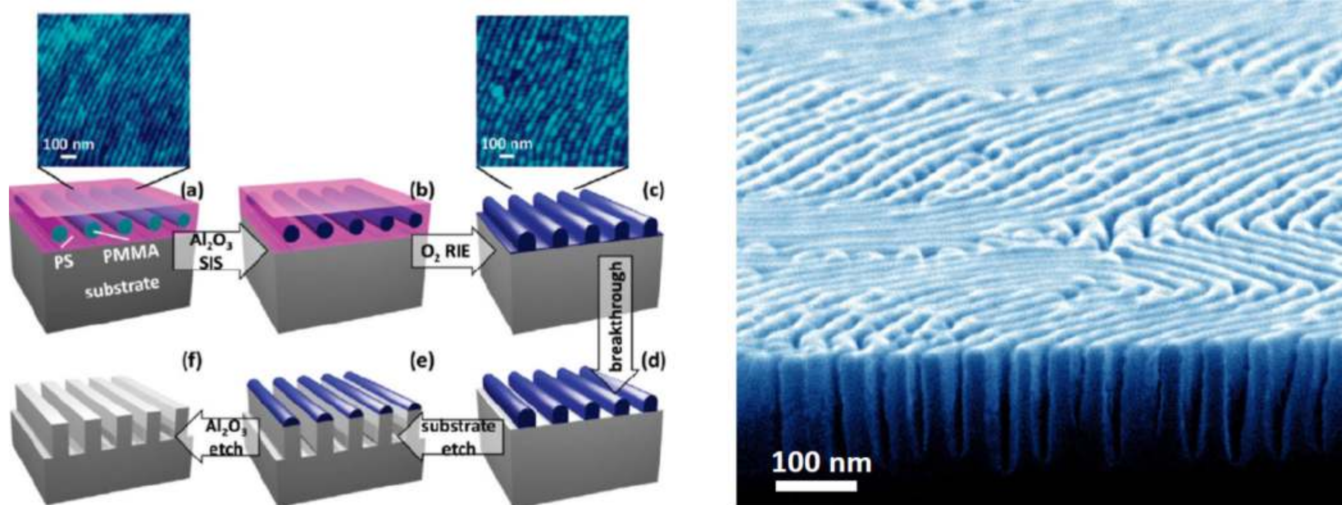

Figure 1.
(Left) SIS lithography using block copolymer. a) Self-assembled PS-b-PMMA thin film and corresponding (AFM vertical scale: 4 nm). b) Al_2O_3 SIS to selectively infiltrate PMMA domains. c) Oxygen plasma to remove unreacted polystyrene phase (AFM vertical scale: 20 nm). d) Break through thin surface alumina layer using BCl_3-based plasma. e) Plasma etch into substrate. f) Removal of mask to reveal nanopatterned substrate. (Right) SEM image of silicon patterned via SIS lithography.

NIST Author Manuscript

NIST Author Manuscript

NIST Author Manuscript

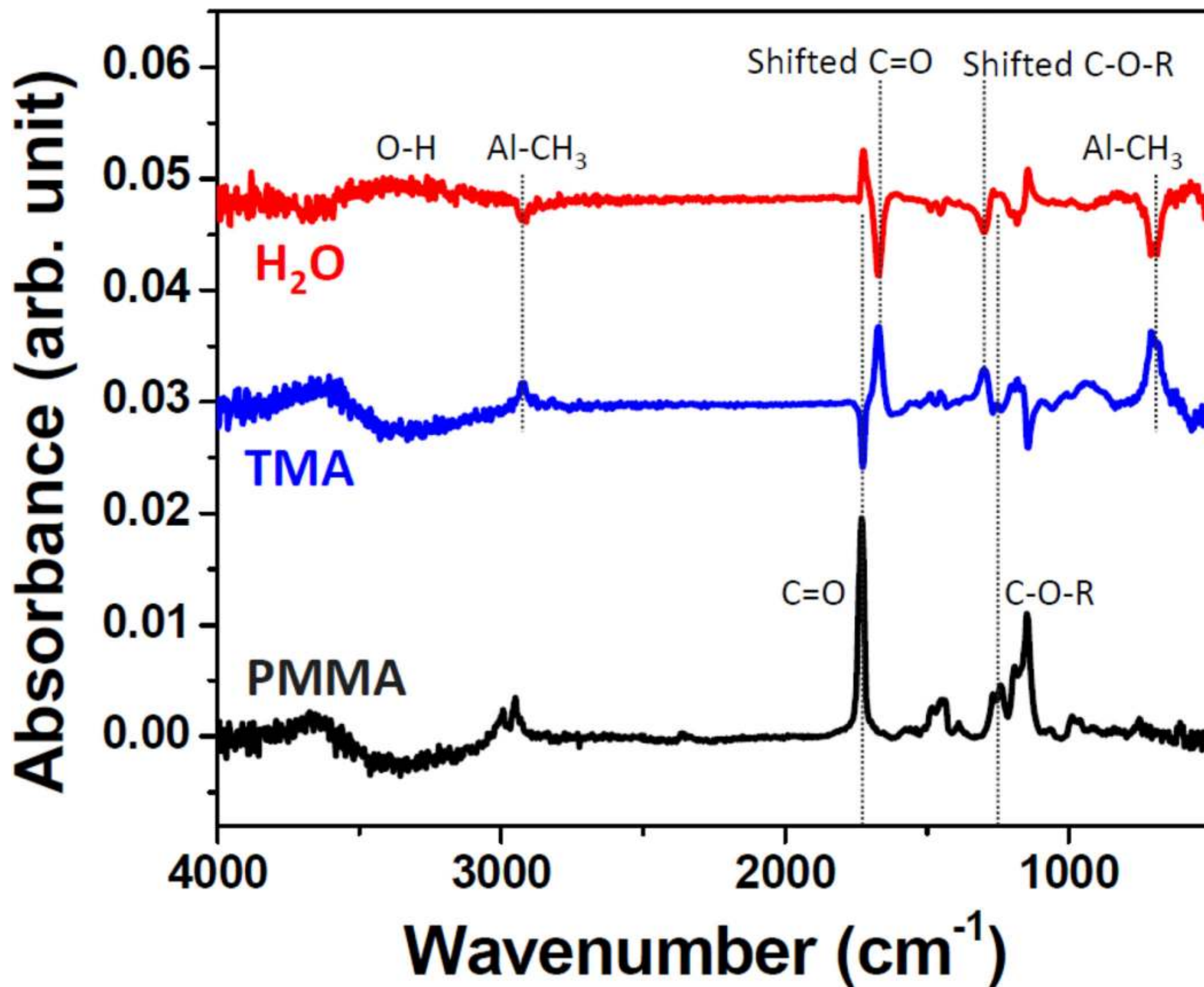

Figure 2.

FTIR spectra recorded during Al_2O_3 SIS into PMMA; (bottom): initial PMMA film; (middle): following TMA exposure referenced to the PMMA spectrum; (top): following H_2O exposure referenced to the TMA spectrum.

NIST Author Manuscript

NIST Author Manuscript

NIST Author Manuscript

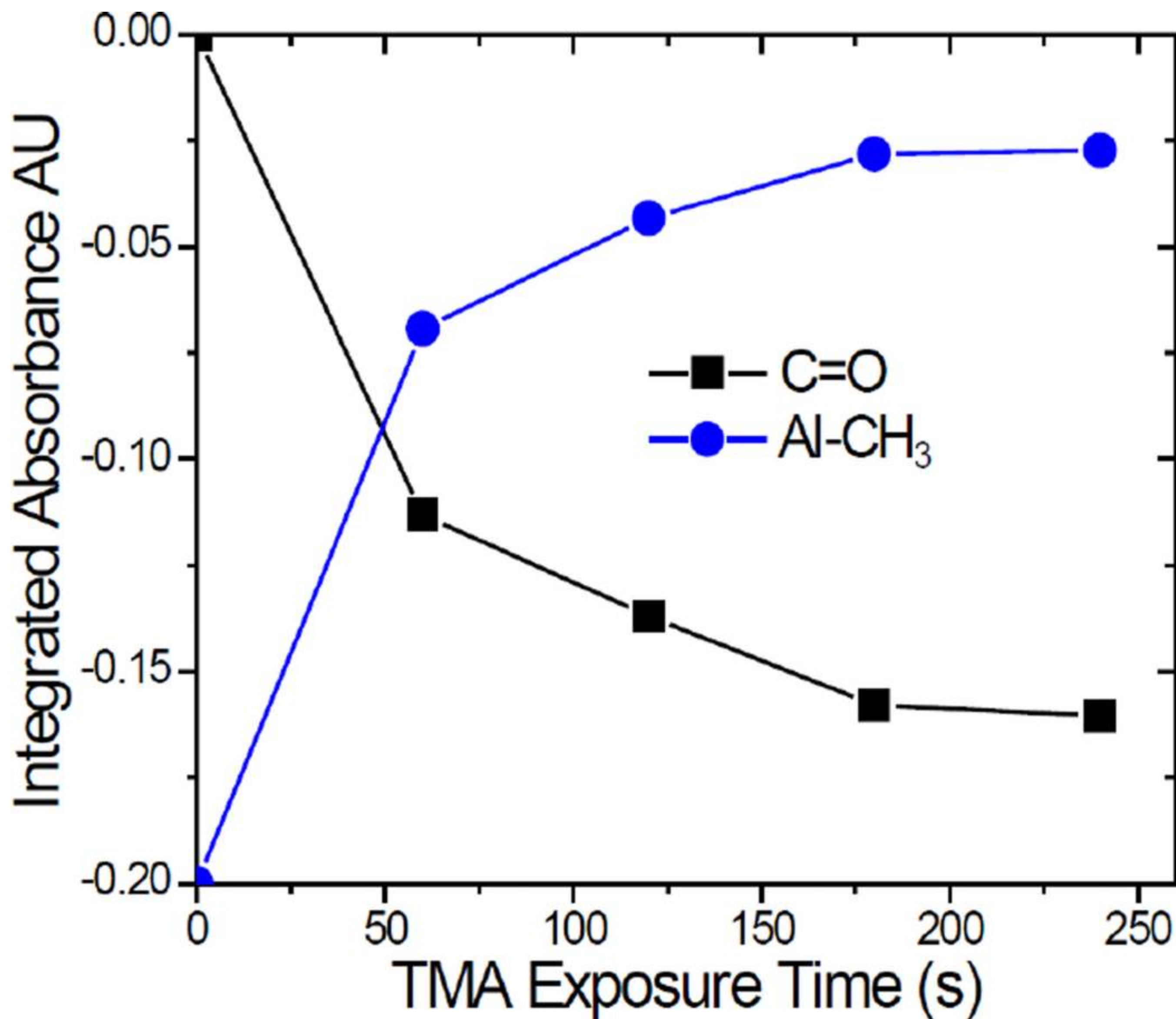

Figure 3.
Integrated absorbance of C=O and Al-CH_3 features in FTIR spectra of PMMA following TMA exposures ranging from 60 to 240 s.

NIST Author Manuscript
NIST Author Manuscript
NIST Author Manuscript

Figure 4.

Proposed mechanism for TMA reaction in PMMA. PMMA and TMA interact rapidly and reversibly to form a weakly-bound complex, but the subsequent reaction to form the covalent structure is slow.

NIST Author Manuscript

NIST Author Manuscript

NIST Author Manuscript

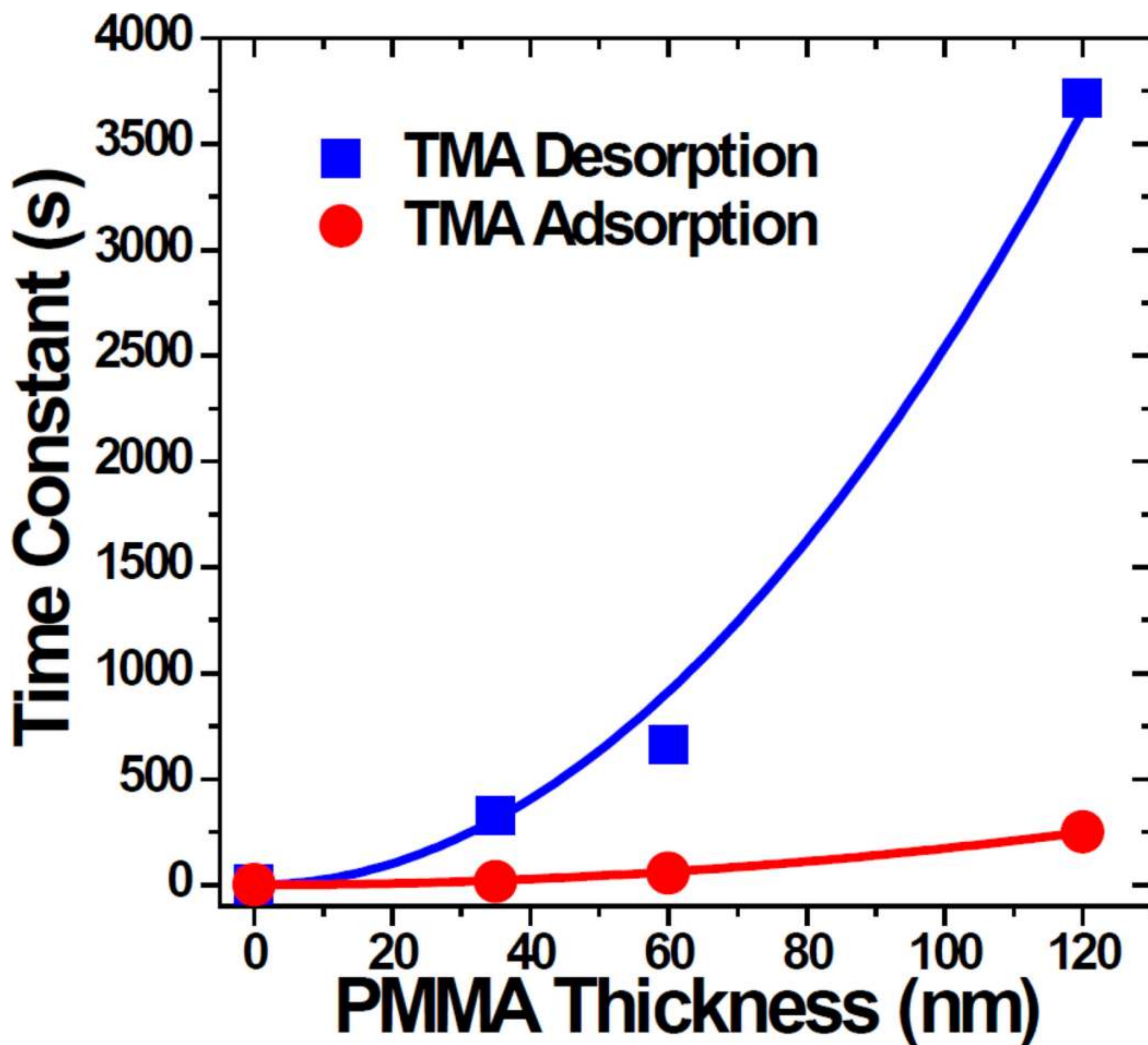

Figure 5.

TMA adsorption (circles) and desorption (squares) time constants versus PMMA film thickness determined from in situ FTIR measurements of the C=O intensity versus TMA exposure and purge times, respectively. Solid lines are quadratic fits to the data points.

NIST Author Manuscript

NIST Author Manuscript

NIST Author Manuscript

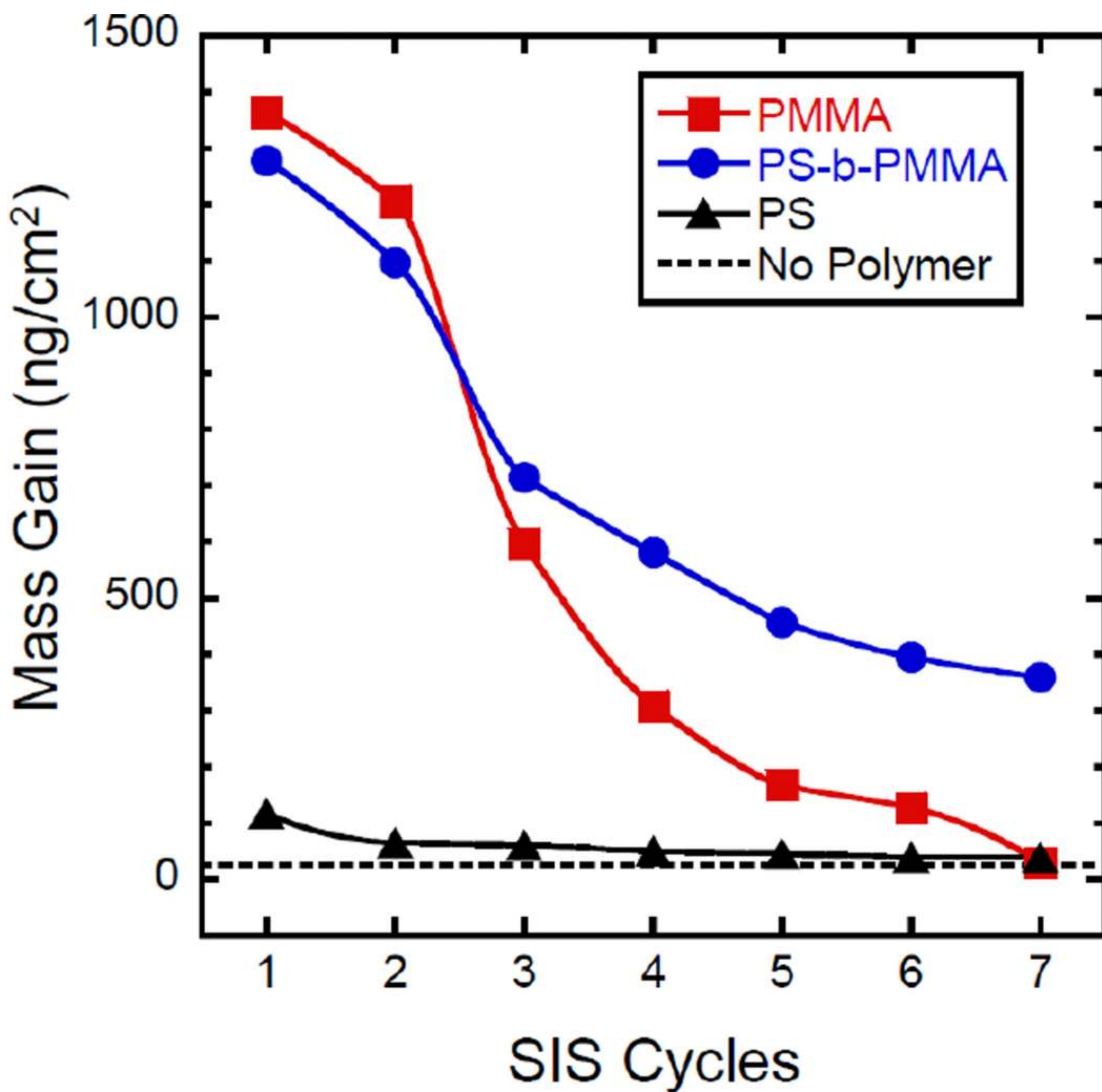

Figure 6.

In situ QCM mass gain measurements versus TiO_2 SIS cycles on QCM sensor crystals pre-coated with 180 nm PS (triangles), 240 nm PMMA (squares), and 280 nm PS-b-PMMA (circles). For reference, the dashed line shows the mass gain expected for an uncoated QCM sensor.

NIST Author Manuscript

NIST Author Manuscript

NIST Author Manuscript

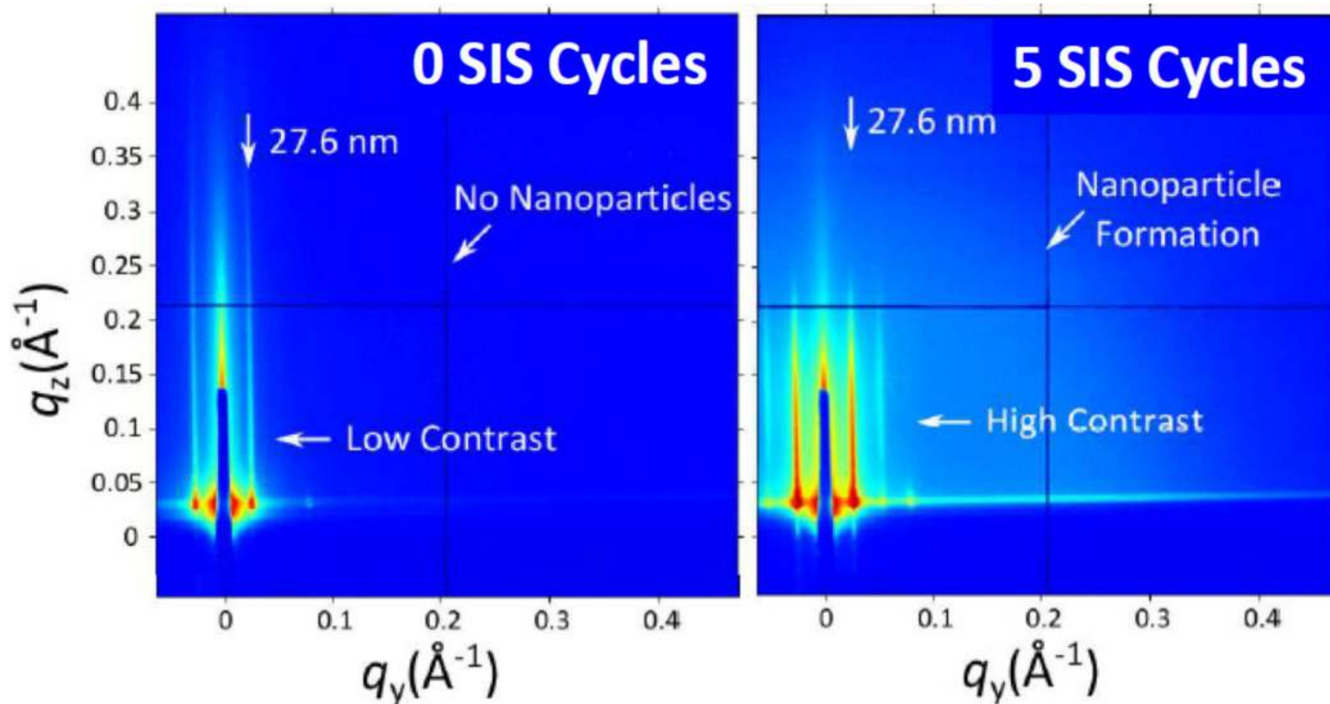

Figure 7.

In situ GISAXS measurements performed during Al_2O_3 SIS into PS-b-PMMA film; (top): initial BC film; (bottom): after 5 SIS cycles

NIST Author Manuscript
NIST Author Manuscript
NIST Author Manuscript

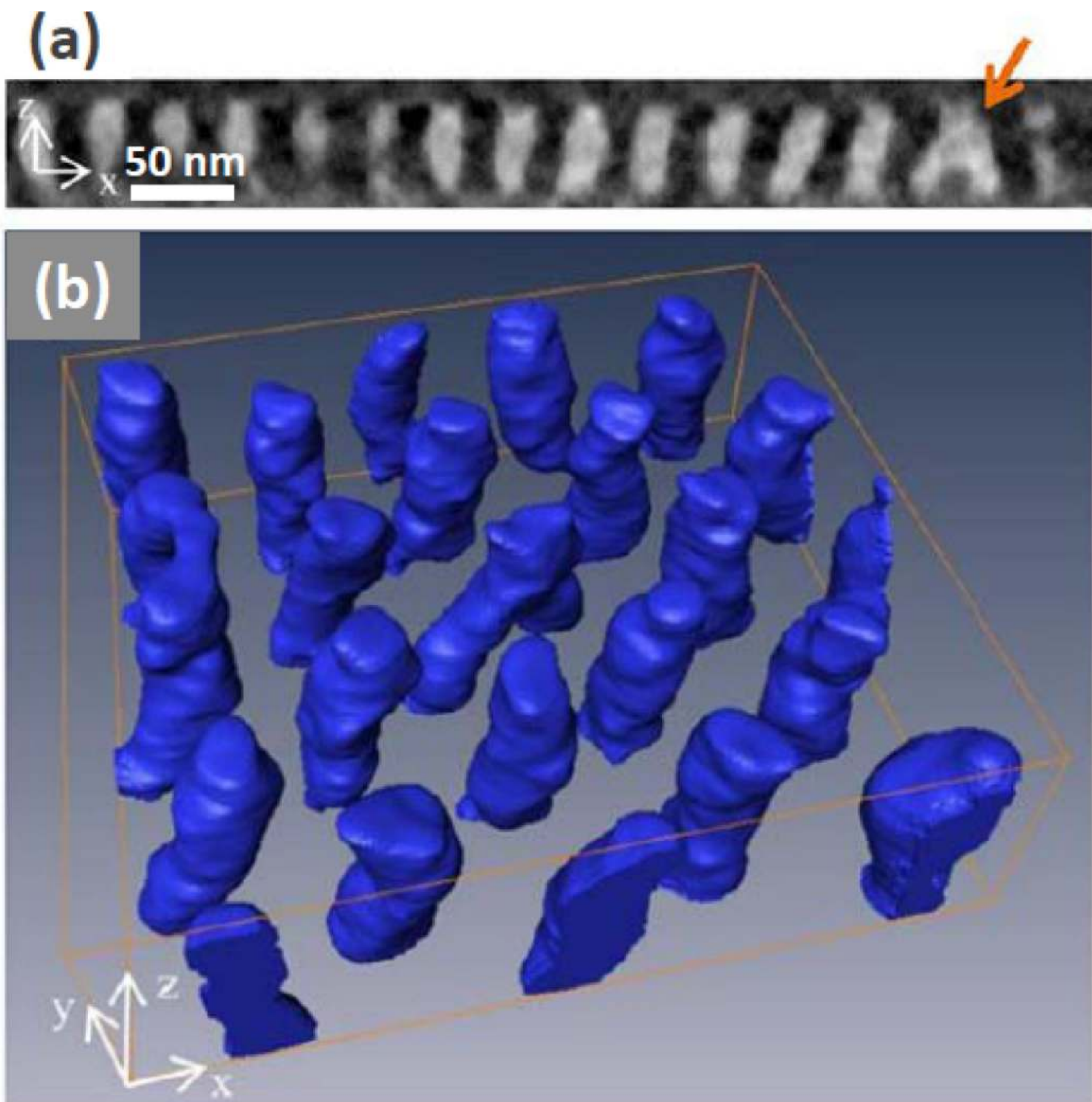

Figure 8.

Three-dimensional structure of a splitting defect in the SIS-treated cylinder-forming PS-b-PMMA film. (a) A 1.1 nm thick xz slice taken at the splitting plane, (arrow points to splitting defect). (b) Visualization of the reconstructed volume of the area of the same defect.